



## Full Length Article

## Comparative study of magnetite nanoparticles obtained by pulsed laser ablation in water and air



Valery A. Svetlichnyi<sup>a,\*</sup>, Anastasiia V. Shabalina<sup>a</sup>, Ivan N. Lapin<sup>a</sup>, Darya A. Goncharova<sup>a</sup>, Tamara S. Kharlamova<sup>a</sup>, Andrey I. Stadnichenko<sup>b,c</sup>

<sup>a</sup> Tomsk State University, Lenina 36, 634050 Tomsk, Russia

<sup>b</sup> Borekov Institute of Catalysis, Lavrentieva 5, 630090 Novosibirsk, Russia

<sup>c</sup> Novosibirsk State University, Pirogova 2, 630090 Novosibirsk, Russia

## ARTICLE INFO

## Keywords:

Pulsed laser ablation in air  
Pulsed laser ablation in water  
Iron oxide  
Surface composition  
Zeta potential  
XPS

## ABSTRACT

Magnetic nanomaterials were synthesized using a method of pulsed laser ablation of an iron target in water (PLAL) and in air (PLAG). The microstructure and composition of the obtained materials differed. Spherical nanoparticles (NPs) of 2–80 nm containing Fe<sub>3</sub>O<sub>4</sub>, α-Fe<sub>2</sub>O<sub>3</sub>, γ-Fe<sub>2</sub>O<sub>3</sub>, FeO and Fe were obtained using PLAL. According to the XPS and FTIR data, the surfaces of these particles contained both Fe<sub>3</sub>O<sub>4</sub> and Fe<sub>2</sub>O<sub>3</sub>. PLAG led to the formation of NPs of 2–120 nm and 2-D lamellar structures up to 1 μm. This material contained more magnetite and nitrogen species, presumably iron nitrides. This material's surface contained FeOOH; the OH-group content was very high. It exhibited the greatest sedimentation stability and zeta potential value, while magnetic NPs (MNPs) obtained in water were less stable in colloids. The difference in the magnetic parameters of the two materials can be connected to not only the different composition (different magnetite content and nitrogen species presence) but also their structural features. Thus, PLAL and PLAG methods allowed for obtaining magnetic nanostructured materials with different characteristics suitable for application in different fields.

## 1. Introduction

Magnetic nanoparticles (MNPs) based on iron-containing compounds, primarily oxides, are of great interest for various applications, as well as for fundamental studies of the effect of their structure, size and morphology on magnetic properties [1–3]. In fields such as biomedicine, for example, magnetite Fe<sub>3</sub>O<sub>4</sub> is preferable to hematite α-Fe<sub>2</sub>O<sub>3</sub> because it exhibits higher residual magnetization [4,5].

There are a number of chemical methods for obtaining MNPs consisting of various iron oxides [6–8]. However, the purity of the final nanomaterials, meaning the absence of the precursors' traces and other contaminants, is important for a number of applications. That is why high-energy physical methods of obtaining MNPs have been intensively developed recently [9–11]. Pulsed laser ablation in a liquid (PLAL) is one of these methods. It has been effectively developing since the '90s [12,13]. PLAL allows one to obtain particles directly in the form of colloids in pure solvents with a minimal amount of precursors, or without them. It also provides the possibility of varying the particles' size and structure within certain limits [14–17]. Recent achievements in understanding the ablation mechanisms and increasing productivity [18–20] have expanded the fields of its practical use, for example, for

catalysis [21–24].

The preparation of iron oxide nanoparticles by PLAL has been studied rather in depth. Varying the parameters of the radiation (wavelength, pulse duration, power), as well as changing the solvent composition, makes it possible to obtain iron oxide particles of different sizes and compositions [25,26,20]. For our group, the synthesis of MNPs by PLAL is the most interesting area [27–30].

NPs with a given composition and structure obtained under pulsed laser ablation in gas (PLAG) or a vacuum is a much less developed technology. Thus, according to the literature data, PLAG of the iron target was carried out under the conditions that predominantly led to hematite α-Fe<sub>2</sub>O<sub>3</sub> nanoparticle formation [31,32]. MNPs for the first time were obtained through nanosecond laser ablation in atmospheric air in our previous work [33].

In previous works, our group studied the composition, structure and morphology of iron oxide nanoparticles obtained by nanosecond pulsed laser ablation of a metallic iron target in air at atmospheric pressure [33] and in distilled water [34,35] using the radiation of the fundamental harmonic of a Nd:YAG laser. These studies showed that NPs obtained through PLAL and PLAG are predominantly composed of magnetite and have similar dimensional characteristics. The main

\* Corresponding author.

E-mail address: [v.svetlichnyi@bk.ru](mailto:v.svetlichnyi@bk.ru) (V.A. Svetlichnyi).

difference of the MNPs obtained in air is the presence of a small amount of nitrogen. Nitrogen, presumably, can present in different forms (iron nitrides, adsorbed nitro and amino groups [33], etc.). Moreover, in addition to spherical NPs, lamellar nanostructures were present in the sample obtained through PLAG.

The aim of this work is a detailed comparative study of the composition and properties of the surface of  $\text{Fe}_3\text{O}_4$  MNPs, depending on the method of obtaining them (PLAL in water or PLAG in air with the same laser source). The surface, along with the size and magnetic and other properties, plays a decisive role in the practical use of MNPs in biology, medicine, catalysis and optoelectronics, which determines the relevance of this study.

## 2. Material and methods

### 2.1. Samples preparation

Iron oxide MNPs were obtained through the ablation of an Fe target (99.5%) by the pulsed focused radiation of an Nd:YAG laser TII LS-2131 M-20 (LOTIS, Belarus) at 1064 nm, 20 Hz, 7 ns and 150 mJ. PLAL and PLAG methods were performed.

- (1) In the case of PLAL, a target with a size of  $40 \times 10 \times 5$  mm was immersed in a 100-ml glass cylindrical reactor filled with distilled water (see the scheme in Fig. 1a). The laser radiation was focused using a short-focus ( $F = 50$  mm) collecting lens. The laser beam was introduced into the reactor through the sidewall. The steam-plasma cloud formed as a result of the target ablation interacted with the solvent. The layer of liquid in front of the target did not exceed 5 mm, minimizing the secondary interaction effects in the colloid between the NPs and the laser radiation. To accelerate the MNPs sedimentation process for additional reduction of the interaction between the NPs and laser radiation, a permanent magnet was installed under the reactor. The ablation process took 3 h. The average yield of MNPs under these experimental parameters was  $\sim 15$  mg/h. The resulting colloids were dried in air at  $50^\circ\text{C}$ . The

synthesis procedure was repeated several times under the same conditions to obtain a sufficient amount of powder for the study. The sample obtained was marked as Fe/water.

- (2) In the case of PLAG, a target with a size of  $40 \times 40 \times 5$  was fixed in a lid on the back end of a cylindrical quartz glass reactor (see the scheme in Fig. 1b). The reactor was 200 mm in length, its internal diameter was 60 mm and it had a volume of  $\sim 565$  cm<sup>3</sup>. The front end of the reactor was closed with a polyethylene membrane transparent for the radiation. The laser beam was focused on the target surface using a long-focus ( $F = 500$  mm) collecting lens. The gas-plasma cloud formed during the target ablation interacted with the molecules of gases from the air. The MNPs obtained settled on the reactor walls, forming a layer of brown powder. To accelerate the MNP deposition process and reduce their interaction with the laser beam, a belt of magnets was fixed around the outside wall of the reactor. The ablation process took 5 h. The powder was then mechanically removed from the reactor walls. The average yield of the MNPs was  $\sim 15$  mg/h. The sample obtained was marked as Fe/air.

In both cases, the initial radiation power density on the target surface was  $400$  MW/cm<sup>2</sup>. For the sake of the uniform irradiation of the target surface, it was automatically moved along the XY plane orthogonal to the laser beam.

There is evidence in the literature that the external electric and magnetic fields can affect the ablation process, the shape and structure of the particles obtained [36–38], and also can structure the obtained particles in a liquid [39]. In the experiments in this work, the permanent magnets were used during the ablation and were set quite far from the irradiation zone. From the TEM and XRD data, we did not find the effect of the magnetic field on the size, morphology, and structure of the nanoparticles obtained. It was found that such use of magnets only led to an increase in the productivity of the particles' obtaining by 1.2 times due to a decrease in the radiation scattering during particles' accelerated deposition.

Additional PLAG in an Ar + O<sub>2</sub> mixture was carried out (for more details, see [33]).

### 2.2. Characterization methods

The characterization was carried out using the equipment of the Tomsk Regional Common Use Centre of Tomsk State University.

X-ray photoelectron spectroscopy (XPS) was performed by using an ES-300 (Kratos Analytical) photoelectron spectrometer equipped with  $\text{MgK}\alpha$  ( $h\nu = 1253.6$  eV) radiation source. The source power was 78 W, so no sample reduction was observed during spectra acquisition. The spectrometer was calibrated using the  $\text{Au}4f_{7/2}$  (84.0 eV) and  $\text{Cu}2p_{3/2}$  (932.7 eV) lines of pure gold and copper metallic surfaces. Spectral calibration for the  $\text{FeO}_x$  samples was performed using  $E_b(\text{C}1s) = 285.2$  eV, typical for carbon impurities on oxide surfaces [22]. Control of the surface chemical composition was attained using survey spectra in the range of 0–1100 eV. The  $\text{Fe}2p$ ,  $\text{Fe}3p$ ,  $\text{O}1s$ ,  $\text{N}1s$  and  $\text{C}1s$  spectral regions were recorded using a pass energy of 25 eV and a 0.1-eV step to study a charge state of the corresponding elements. The chemical composition of surface was quantitatively determined from integral peak areas using standard atomic sensitivity factors (ASF) [39]. Processing of the obtained data and spectral analyses (curve fitting, area calculation, and difference spectra) were performed using the XPS-Calc program, which has been tested on a number of systems [40–42]. The curve fitting procedure was performed using an approximation based on a combination of the Gaussian and Lorentzian functions with subtraction of a Shirley-type background. Before the curve fitting, all experimental spectra were smoothed using a Fourier filter. No considerable difference between the smoothed and experimental curves was observed; the mean-square deviation was less than 1%. The maximum depth of XPS analysis is limited by 3-fold inelastic mean free path

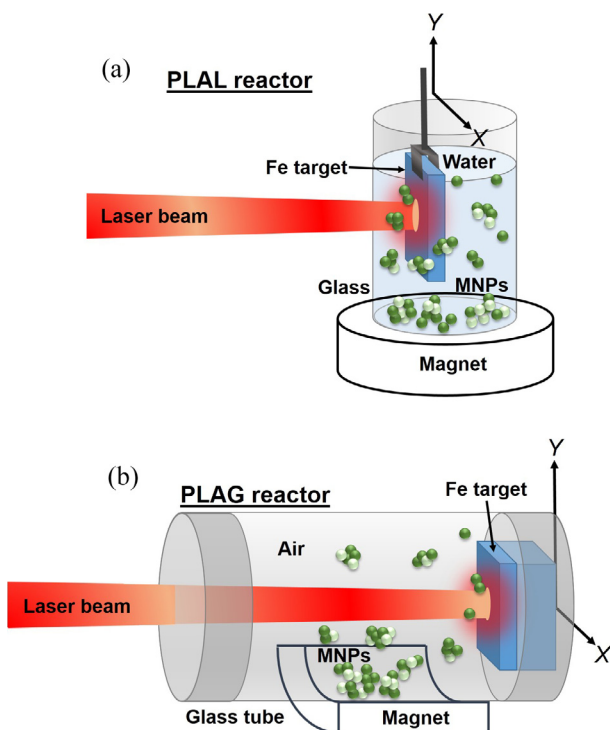


Fig. 1. Scheme of experimental setup for MNP synthesis by PLAL (a) and PLAG (b).

(IMFP) –  $3\lambda$ . The IMFP values for Fe3p, O1s and Fe2p photoelectrons emitted from FeO<sub>x</sub> were calculated as 9–7 nm [43]. Therefore, the depth of XPS analysis of FeO<sub>x</sub> samples can be considered as a layer with thickness less than 9 nm.

To study the electrokinetic characteristics of the Fe/water and Fe/air powders, aqueous suspensions of the samples with a concentration of 20 mg/l were prepared. The powders were ultrasonicated (a bath of 500 ml, at 35 kHz and 50 mW) in a 100-ml beaker with distilled water three times for 10 min. The sample obtained through PLAL was also studied in the form of the initial colloid (Fe/water<sub>init</sub>).

Zeta potential values of the particles were determined through electrophoretic light scattering with phase analysis (PALS) using a Nano Brook Omni (Brookhaven, USA). To study the dependence of the particles' zeta potential on the pH of the dispersion, the initial colloids were titrated with the diluted (0.001 and 0.1 mol/l) aqueous solutions of KOH or HNO<sub>3</sub> using a BI-ZTU automatic titrator (Brookhaven, USA).

Raman spectra of the powder samples were obtained using an InVia (Renishaw, UK) confocal Raman dispersion spectrometer equipped with a Leica microscope with a 50 × objective. Excitation was performed with a semiconductor laser at 785 nm and 100 mW. To prevent sample heating and phase transformation [35,44], only 0.5% of laser power was employed with the 100% defocusing mode. The Raman spectra were measured in the 100–1000 cm<sup>-1</sup> range with a 1 cm<sup>-1</sup> spectral resolution. Powder samples were examined through ATR-FTIR spectroscopy (Nicolet 6700, Thermo Fisher Scientific, USA) in the range of 400–4000 cm<sup>-1</sup> with a 4 cm<sup>-1</sup> spectral resolution. Reflection spectra were converted using Kubelka–Munk transformations.

The BET surface area of the powders was measured using a gas-adsorption analyzer of specific surface area and porosity, TriStar II 3020 (Micromeritics, USA). Before analysis, the powder samples of the material were degassed in a vacuum (10<sup>-2</sup> Torr) at 200 °C for 2 h.

The magnetic properties of the materials were studied at room temperature using a vibrating sample magnetometer (VSM) in a magnetic field up to ± 20 kOe. Mechanical vibrations of the sample were provided by a vibrator of the original design. The relative instability of the oscillation amplitude was 10<sup>-4</sup>, with a frequency of 10<sup>-5</sup>. For the signal registration, the system of four pickup coils was used. The dynamic range of the equipment was 5 × 10<sup>-6</sup>–100 emu. The KBr powder was used to ground the samples and press them into the tablets for the magnetic measurements. More details on the experiment can be found in our previous work [35].

### 3. Results and discussion

#### 3.1. Microstructure study

The materials obtained were studied through TEM. Fig. 2 presents the obtained images with the additional HRTEM insets. The samples contain different structural elements. The Fe/water sample consists of agglomerated spherical or near-spherical crystalline particles (Fig. 2a). The largest particles are up to 80 nm in size, but the main fraction is presented by the NPs of 1–10 nm in size, with the maximum of distribution at 2 nm [35]. The Fe/air sample is represented by three different structures. First are 2-D thin (up to 10 nm) sheets of 1 μm in length/width, so-called lamellas. They seem to be composed of small crystal or amorphous particles of 1 nm or smaller (Fig. 2b, upper right corner inset). The second structural element in this sample are rolls (Fig. 2b, upper left corner inset) that are formed by the twisted lamellas. Their width can reach 150 nm. The third structures that can be found in the Fe/air sample are spherical and near-spherical crystal NPs of 2–120 nm (Fig. 2b, two lower left insets), with the maximum size distribution at 12–15 nm [33].

The BET data obtained for the samples at the preliminary degassing at 200 °C are presented in Table 1. One can notice that the specific surface areas for both samples are relatively close in value. However, the pore volume and pore size for the Fe/air sample are almost twice as

low as those of the other sample. That can be explained by the microstructure of this sample—almost half of its mass is represented by lamellar structures that may contain smaller pores (their structural elements are extremely small), but since the lamellas are 2-D, the pore volume is not expected to be high.

Thus, it is seen that the media for the PLA process dramatically affects the product microstructure.

#### 3.2. Composition study

##### 3.2.1. X-ray diffraction

The XRD patterns for the samples are presented in Fig. 3. Because iron oxide phases exhibit quite close peak positions, the task of determining precise sample phase compositions is almost impracticable. However, a relative estimation can be carried out.

It is seen that the Fe/air sample pattern contains mainly magnetite signals (~90%), and small iron nitride (Fe<sub>2</sub>N) peaks can be identified (~1.5%). It almost does not exhibit maghemite and hematite peaks (the total signal from the remaining phases is less than 9%). The XRD pattern of the Fe/water sample, on the contrary, contains peaks of maghemite and hematite (about 10%), magnetite (~74%) and, moreover, peaks of FeO (~15%) and the metallic Fe (~1%).

Thus, not only the microstructure but also the phase composition of the samples obtained in water and air media differ. Despite the fact that the main phase of both samples is magnetite, the Fe/water sample contains significantly more impurities of other iron-based phases.

##### 3.2.2. Raman spectroscopy

It is known that the Raman spectra registration should be carried out under soft conditions in order to avoid phase transformations in the samples [35,44]. The spectra obtained under such conditions are presented in Fig. 4. It is seen that, according to Raman data, both the samples contained magnetite phase only: 668 (A<sub>1g</sub>), 538 (T<sub>2a</sub>), and 306 (E<sub>g</sub>) [39].

XRD analysis is based on integrated signal obtaining, while Raman deals with local near-surface analysis. Thus, other phases may be not seen because of their low content. Also, the conditions for the Raman spectra registration were chosen to be soft in order not to damage the sample. That is why the sensitivity may be too low to distinguish the small amount of, for example, nitride in the spectra.

##### 3.2.3. X-ray photoelectron spectroscopy and IR spectroscopy

The carbon C1s peak at 285.2 eV was used as a reference for the charge correction (Fig. S1, Supplementary Material). Carbon is a common contaminant appearing in the XPS data. Because the samples were kept in air, the carbon-containing species have adsorbed on their surface. Moreover, the Fe/air sample was obtained in air, and the carbon content on its surface was twice as high as that of the Fe/water sample (Table 2).

The analysis of Fe2p lines (Fig. 5a) provided the following information. For the Fe/water sample, peaks for Fe<sub>3</sub>O<sub>4</sub> (at 710.9 and 724.4 eV for Fe2p<sub>3/2</sub> and Fe2p<sub>1/2</sub>, respectively) were found, along with a satellite at 718.8 eV that is more typical for Fe<sub>2</sub>O<sub>3</sub> [45]. For the Fe/air sample, these lines were shifted, and the satellite line almost disappeared. The line at 711.6 eV corresponds to FeOOH [46].

Using the Fe3p line (Fig. 5b), the Fe/air sample was found to contain Fe<sup>3+</sup> on the surface. It is characterized by the binding energy of 56.4 eV. According to McIntyre [46] and Yamashita [45], this line corresponds to FeOOH. In the Fe/water sample, the Fe3p line can be decomposed into two components obtained at 53.7 and 55.7 eV (Fig. S2, Supplementary material). The first corresponds to Fe<sub>3</sub>O<sub>4</sub> [46], and the second one is typical of Fe<sub>2</sub>O<sub>3</sub>.

Nitrogen was detected in the Fe/air sample (Fig. 6a). Two nitrogen N1s components were found with binding energies of 400.0 and 407.0 eV. The nitrogen component at 400 eV could belong to either the NH<sub>3</sub>, NH<sub>2</sub>-group or to iron nitride Fe-N<sub>x</sub>. Another N1s component (at

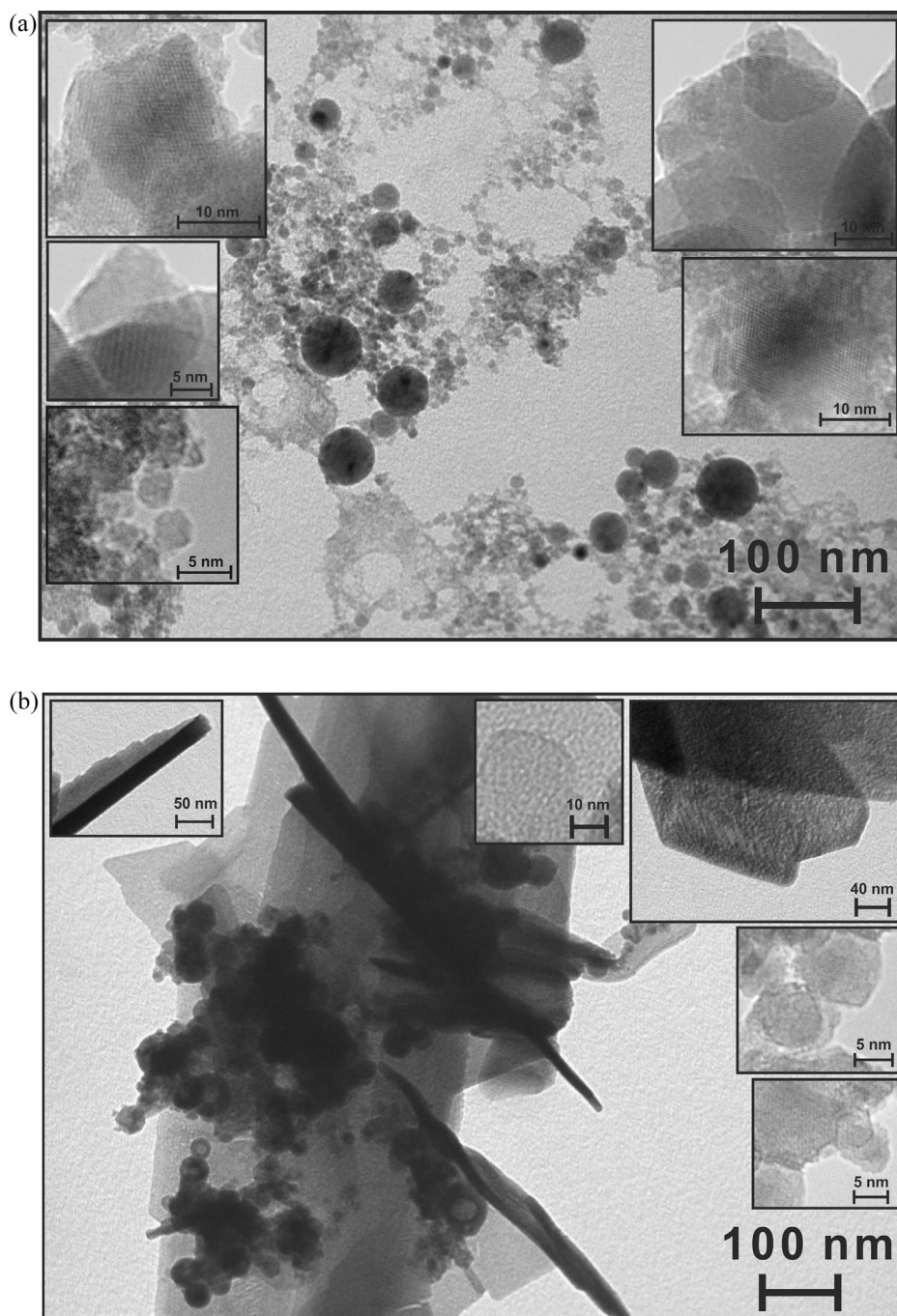


Fig. 2. TEM images with HRTEM insets for Fe/water (a) and Fe/air (b) samples.

**Table 1**  
BET data for the samples.

Sample	$S_{\text{BET}}$ [ $\text{m}^2/\text{g}$ ]	Pore volume [ $\text{cm}^3/\text{g}$ ]	Average pore diameter [nm]
Fe/air	100.8	0.114	4.5
Fe/water	121.4	0.209	6.9

407 eV) more likely concerns the nitrogen from the nitro-group  $\text{NO}_3$ . These data are consistent with the ATR-FTIR spectra, pointing at both nitrogen components' presence (Fig. S3). In our previous work [33], the  $\text{NH-}$  and  $\text{NH}_2$  groups were found in the Fe/air sample (vibrations at 700–850 and 1550–1650  $\text{cm}^{-1}$ ), along with  $\text{NO}_2$  species (1260–1390 and 1490–1660  $\text{cm}^{-1}$ ).

To better understand the source of nitrogen presence on the Fe/air

surface, the Fe/Ar +  $\text{O}_2$  sample was obtained through PLAG in the argon-oxygen mixture. According to XPS, this sample also contained nitrogen on the surface (Fig. S4), but the ratio N/Fe, in this case, was twice as low as for the Fe/air sample. Because iron nitrides were not found in SAED patterns for the Fe/Ar +  $\text{O}_2$  sample [33], it was concluded that N presented in this sample only in adsorbed form on the surface. This was confirmed by the FTIR data (Fig. S3). Vibrations at 1454 and 1620  $\text{cm}^{-1}$  correspond to  $\text{N=O}$  monomers and at 1343  $\text{cm}^{-1}$  to  $\text{N=O}$  dimers. As mentioned above, the Fe/air sample spectrum contained both NO and NH bond vibrations (Fig. S3 and [33]). Also, the Fe/air sample contained more nitrogen, and the nitrogen-containing phases can be detected by the XRD (Fig. 3 in Section 3.2.1.) and SAED (our previous work [33]). Thus, it can be assumed that the NO-containing species can adsorb onto the material surface after the ablation

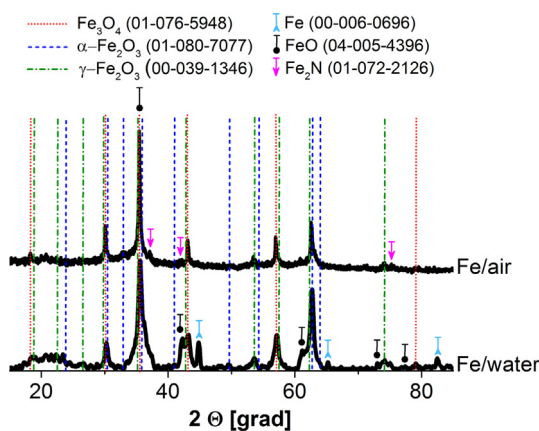


Fig. 3. XRD patterns for Fe/water and Fe/air samples.

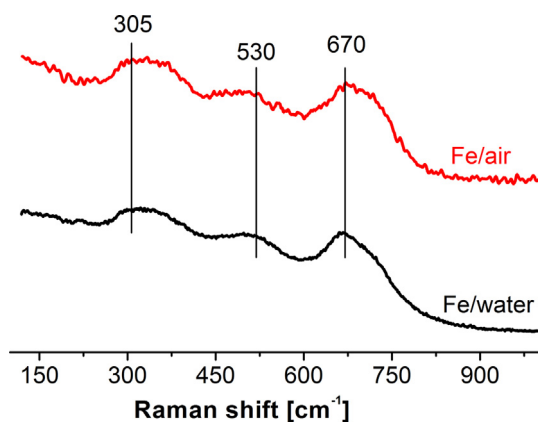


Fig. 4. Raman spectra for Fe/water and Fe/air samples.

Table 2

Data on the samples' surface composition calculated from the XPS analysis.

Sample	Atomic concentration [%]			
	C	O	N	Fe
Fe/water	22.0	44.9	–	33.1
Fe/air	42.9	41.2	3.9*	12.0

\* 1.0% for N-H and 2.9% for N-O.

because the Ar + O<sub>2</sub> atmosphere excluded sample interaction with nitrogen during the PLAG process. Also, it should be mentioned that the Fe/water sample did not contain nitrogen on the surface, so this sample, when in the form of a powder, is stable to the nitrogen sorption. At the same time, nitrogen present in the crystal lattice of the Fe/air nanostructures makes it different from the Fe/water sample in terms of fields of application and affects its surface properties.

The analysis of the O1s line showed that the oxygen state in the Fe/water and Fe/air samples differed as well (Fig. 6b). The binding energy of 530.0 eV for the sample ablated in water corresponds to O from FeO, γ-Fe<sub>2</sub>O<sub>3</sub> or Fe<sub>3</sub>O<sub>4</sub>. The O1s line for the sample ablated in air is deconvoluted (not shown) to two components at 530.8 and 532.4 eV. According to the literature [46], these binding energies are characteristic of FeOOH. Yamashita and Hayes [45] also mentioned that oxygen from the OH-group exhibited a line at 532.2 eV. The significant amount of OH-groups on the Fe/air sample surface was also confirmed by ATR-FTIR data (Fig. S3). The broad peak at 3000 cm<sup>-1</sup> corresponds to O–H vibrations. It exceeds the amount of surficial OH-groups in the Fe/water and Fe/Ar + O<sub>2</sub> samples that is consistent with what was mentioned above (see Fe XPS lines analysis).

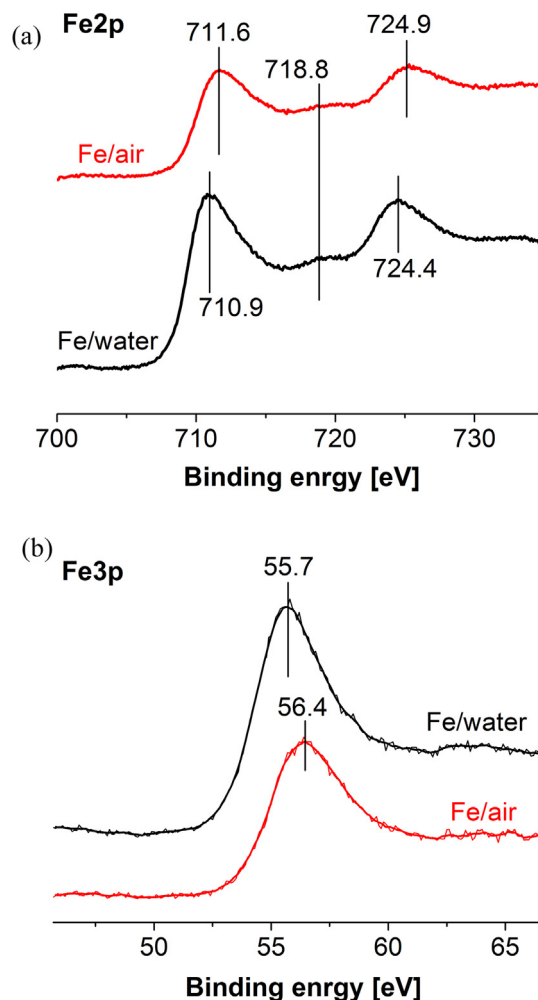


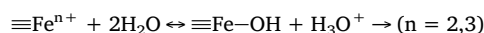
Fig. 5. XPS lines Fe2p (a) and Fe3p (b) for Fe/water and Fe/air samples.

Thus, it can be concluded that the surface composition of the samples is completely different (Table 2). The Fe/O ratio is seen to be 0.7 and 0.3 for Fe/water and Fe/air, respectively. This atomic ratio is 0.75 for Fe<sub>3</sub>O<sub>4</sub>, 0.67 for Fe<sub>2</sub>O<sub>3</sub> and 0.5 for FeOOH. Thus, such results can be explained by the presence of FeOOH on the Fe/air sample surface that was confirmed by both XPS and ATR-FTIR. Additionally, the presence of nitrogen-containing compounds (both Fe–N and O–N) can explain the deviation of the Fe/O ratio from 0.5 to 0.3.

Thus, in addition to the information on the surface composition of the samples, the results obtained by XPS and FTIR can be used to understand the properties of the corresponding colloids, such as point of zero charge, stability, pH, etc.

### 3.3. Electrokinetic study

The distilled water used for the colloid preparation was characterized by a pH of ~6 due to the carbon dioxide dissolution from the air during storage. The colloids obtained exhibited pH values from 4 to 6 and positive zeta potential values (Table 3). The pH values observed were caused by the hydration of the particles' surface accompanied by hydrolysis and subsequent surface ionization. In particular, the hydration of the iron oxide particles' surface led to a dissociative adsorption of water on surface iron cations with the formation of the surface hydroxyl groups. The resulting proton can go into the liquid phase, changing the pH of the colloid:



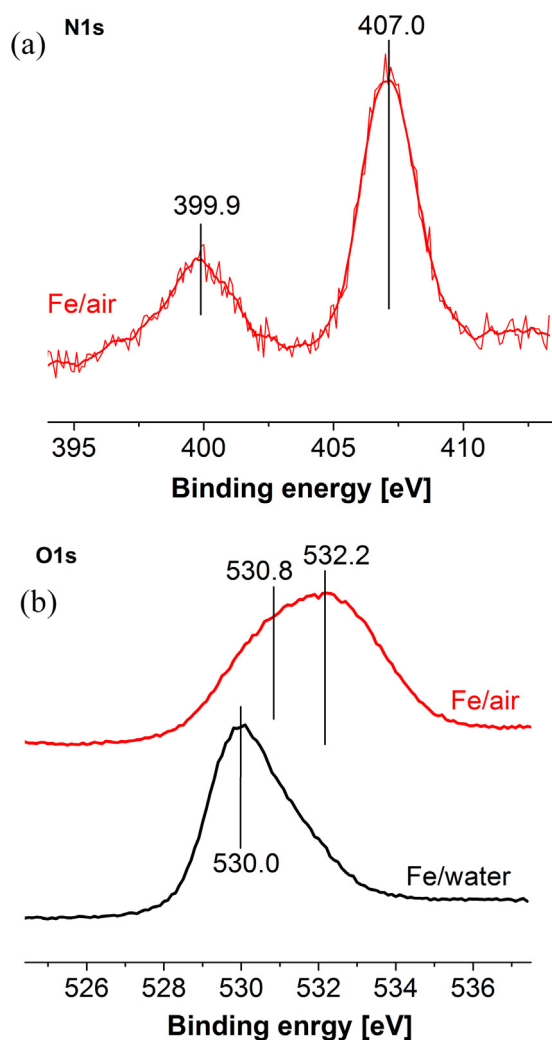


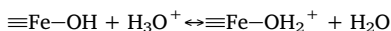
Fig. 6. XPS N1s (a) and O1s (b) lines for the samples.

Table 3

The data obtained through the colloid titration.

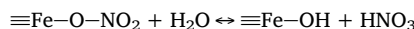
Sample	Initial pH	Initial zeta potential [mV]	pH <sub>IEP</sub> direct titration	pH <sub>IEP</sub> back titration
Fe/water	5.5	+16.8	6.2	2.7
Fe/water_init.	6.03	+21.7	6.7	3.2
Fe/air	4.08	+36.2	7.2	6.4

Alternatively, H<sup>+</sup> can participate in the surface ionization, determining the surface potential:



In the case of the Fe/water\_init. sample (the colloid after PLAL), the pH was caused by the processes taking place during the PLAL and the subsequent aging of the particles in the supernatant solution, including surface ionization that determines the surface potential.

The lowest pH value was determined for the Fe/air colloid. This fact points to the presence in its particles of more surface centers available for the hydration, in contrast to the sample obtained in water (meaning Fe/water that was dried and dispersed in water again for the zeta potential measurement). In the sample obtained in air, according to ATR-FTIR spectroscopy (see Section 3.2.3 and [33]), there were surface NO<sub>3</sub>-groups/iron nitrates, which can readily be hydrolyzed to form nitric acid:



Thus, the presence in the samples of surface NO<sub>3</sub>-groups/iron nitrates causes a more acidic medium of the resulting colloid. This leads to a high zeta potential value of the particles and colloid stabilization (the colloid was found to be stable for several weeks).

The colloid of the Fe/water sample exhibited a relatively high pH, a low zeta potential (below +20 mV) and low stability. The initial colloid (Fe/water\_init.) obtained directly through the PLAL of iron in water, despite the relatively high pH, was characterized by a large zeta potential. It exhibited greater stability than the dispersion of the Fe/water sample. It can be associated with a smaller particle size and a large number of surface functional groups in the case of iron oxides formed in water. The Fe/water colloid was obtained through the separation from the colloid followed by the drying. Therefore, the change in its particle characteristics can be associated with a change in the particles' surface state. The initial hydrated sample restructured its subsurface layer during drying. The dehydration process, including oxolation (surface hydroxide interaction with the formation of water and the Fe–O–Fe bond), is accompanied by the transition of Fe (II) to Fe (III). During the drying process, the formation of rigid agglomerates of the particles occurs due to the inter-particle interaction of the surface hydroxides.

Fig. 7 shows the curves of the direct (by the KOH solution) and back (by the HNO<sub>3</sub> solution) titrations. The dependences of the potential on the pH of the colloid obtained for the direct titration for all the samples are quite similar. The pH values at the zero-charge point for the samples studied are in the range of 6.2–7.2, which is characteristic of magnetite Fe<sub>3</sub>O<sub>4</sub> [42] and agrees well with the data of XRD and Raman spectroscopy. At the same time, the pH at the zero-charge point for the Fe<sub>2</sub>O<sub>3</sub> oxide lies in the same interval [47]. A small but obvious difference in pH<sub>IEP</sub> for the samples obtained in water and gas indicates a difference in the surface state of the samples obtained through different methods.

It is noted in [47] that the magnetite Fe<sub>3</sub>O<sub>4</sub> with the different Fe (II)/Fe (III) ratio is characterized by the different pH<sub>IEP</sub> values: for Fe (II)/Fe(III) = 0.45, pH<sub>IEP</sub> is 6.6, but for Fe(II)/Fe(III) = 0.35, pH<sub>IEP</sub> is 7.2. Thus, the data of the electrokinetic study indicated that the surface composition of the samples obtained in water and the gas phase is different, which may be the reason for the different stability of the resulting suspensions. That is consistent with the XPS and FTIR data (see Section 3.2.3.).

The course of the back titration curves depends on the method of obtaining the samples, which further confirms the difference in the composition of their surface. For the Fe/air sample obtained in the gas phase, a slight hysteresis was observed (Fig. 7b). This is due to a relatively high rate of the titration of the colloid by the acid that is insufficient to establish equilibrium. At the same time, for the Fe/water and Fe/water\_init. Samples obtained in water, under the same titration conditions, more pronounced hysteresis was observed (Fig. 7a, c). This indicates that deeper conversions occurred when the acid was added to the system. In particular, these may be partial dissolution processes, characteristic of Fe<sub>3</sub>O<sub>4</sub> in diluted acids accompanied by a strong change in the composition and structure of the surface. The Fe/air sample contained magnetite as well, but the FeOOH and OH-groups on its surface (according to XPS and FTIR data) may have protected it from dissolution.

In general, it can be assumed that in the case of the Fe/air sample obtained in the gaseous phase, the surface of the Fe<sub>3</sub>O<sub>4</sub> particles (or the resulting oxide as a whole) is characterized by a higher Fe(III) content, while for the samples obtained in water, the amount of Fe(III) on the surface was lower. For the Fe/air sample, a more thermodynamically stable hematite Fe<sub>2</sub>O<sub>3</sub> with a defect spinel structure on the Fe<sub>3</sub>O<sub>4</sub> surface is possible. This completely agrees with the XPS data.

Thus, the medium used for the pulsed ablation affects the MNPs surface charge state. The most stable sample obtained through PLAG showed lower initial pH and higher zeta potential. This can be

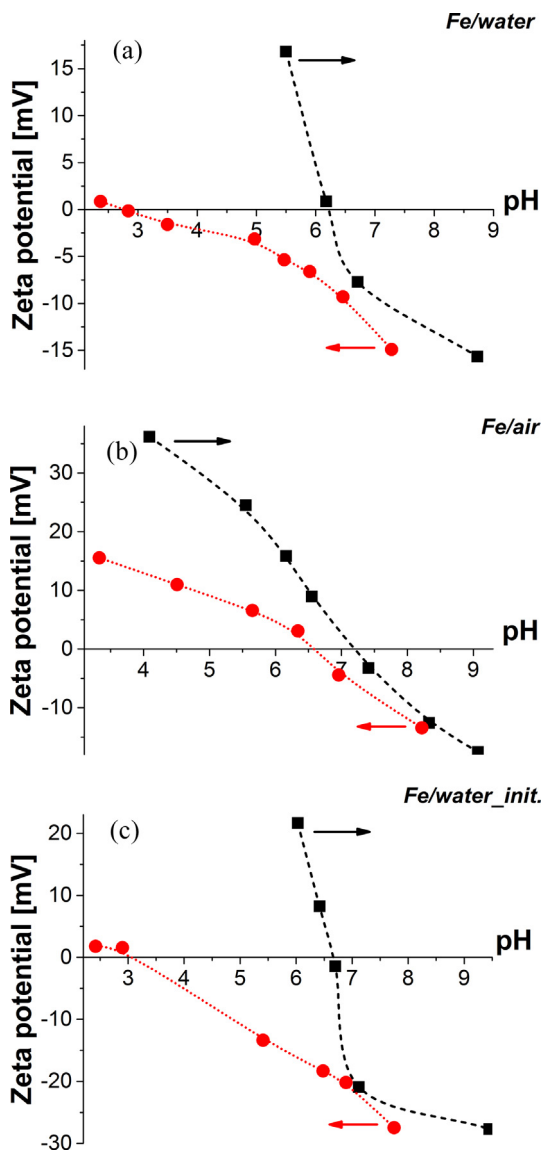


Fig. 7. Zeta potential dependence on the pH for the (a) Fe/water, (b) Fe/air, (c) Fe/water\_init. samples at the direct (black color) and back (red color) titration.

explained by both the presence of the nitrogen species on its surface and the surface FeOOH content (see XPS data), so the surface OH-groups can additionally stabilize the particle colloids. The Fe/water sample exhibited lower but still sufficient stability. Its surface had a higher Fe (II)/Fe(III) ratio, which can provide other functional properties that are in demand, for example, in biomedicine and sensorics.

### 3.4. Magnetic properties study

VSM data obtained for the Fe/water and Fe/air samples are presented in Fig. 8 and Table 4. A hysteresis loop was observed at the magnetization curves for both the materials at room temperature. The shape of the loop is characteristic of ferromagnetic particles.

The samples exhibited almost equal remanent magnetization ( $M_r$ ), but the magnetization of saturation ( $M_s$ ) and coercivity ( $H_c$ ) differed.  $H_c$  is a size-dependent parameter. Because the Fe/water sample consisted of smaller particles, it should have exhibited lower coercivity. However, the effect was contra verse. The Fe/air sample contained lamellas consisting of very small structural elements. This may have led to the higher  $H_c$  value of the Fe/water sample. Also, the higher the defective structure of the material, the higher the  $H_c$  value [48]. Thus, the

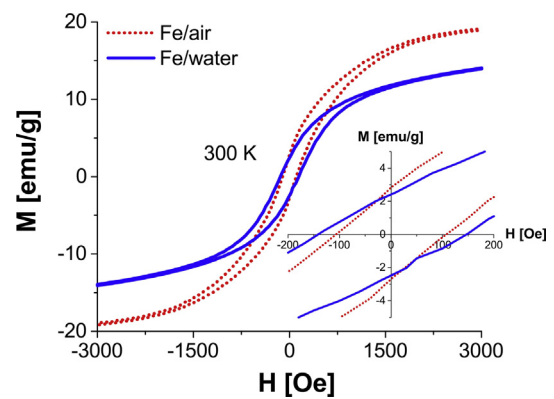


Fig. 8. VSM data for Fe/water and Fe/air samples.

Table 4  
VSM data of the samples.

Sample	$M_r$ [emu/g]	$M_s$ [emu/g]	$H_c$ [Oe]
Fe/water	2.5	15	145
Fe/air	2.8	20	100

particles of the Fe/water sample may contain more defects, strains, dislocations, etc. The  $M_s$  of the samples may differ because of the different magnetite content as well as the nitrogen presence in the Fe/air sample. It is known that the magnetic properties of the iron nitrides differ from those of the oxides. Thus, iron nitrides contribute to the differences in magnetic properties, as well as the structural difference of the samples.

### 4. Conclusions

Iron-based magnetic nanomaterials were synthesized using pulsed laser ablation in water and air. The samples obtained were studied and compared.

It was found that not only the microstructure but also the phase composition of the samples obtained in water and air media differed.

Iron ablated in water consisted of spherical and near-spherical NPs 2–80 nm in size (maximum of 2 nm) of magnetite (74%) with other oxide phases and metallic iron. The surface of these particles contained both  $\text{Fe}_3\text{O}_4$  and  $\text{Fe}_2\text{O}_3$ . Ablation of iron in air led to the formation of NPs 2–120 nm in size (maximum of 12–15 nm) and 2-D lamellar structures up to 1  $\mu\text{m}$ . This material contained more magnetite phase than the Fe/water sample (90%), and nitrogen species were detected both adsorbed and in the composition of the crystal phase, presumably iron nitrides. Under ablation in air, the surface of the obtained materials contained FeOOH, and the OH-groups content was very high.

The material obtained through PLAG exhibited the greatest stability and zeta potential value. It was assumed that the nitrogen species and OH-groups on its surface stabilized the colloids of this material. The sample ablated in water exhibited lower but still sufficient stability. Its surface had a higher Fe(II)/Fe(III) ratio that can provide other functional properties.

The samples' magnetic behavior was found to be quite similar. However, the sample obtained in air exhibited larger magnetization of saturation and lower coercivity. It was assumed that the difference in the parameters could be connected to not only the different sample compositions (different magnetite content and nitrogen species presence) but also their microstructure difference.

Thus, pulsed laser ablation in water and air allows one to obtain magnetic nanostructured materials with different characteristics. This is quite important for the material application in various fields, such as biomedicine, sensorics and catalysis.

## Acknowledgments

This work was supported by the Ministry of Education and Science of the Russian Federation, Project Number 3.9604.2017/8.9. The authors express their appreciation to A.E. Sokolov and D.A. Velikanov from Kirensky Institute of Physics (Krasnoyarsk, Russia) for the VSM measurements. Also, the authors thank the service Proof-Reading.com for the English text improvement.

## Appendix A. Supplementary material

Supplementary data to this article can be found online at <https://doi.org/10.1016/j.apsusc.2018.10.189>.

## References

- [1] S. Bagheri, N. Muhd Julkapli, Modified iron oxide nanomaterials: Functionalization and application, *J. Magn. Mater.* 416 (2016) 117–133, <https://doi.org/10.1016/j.jmmm.2016.05.042>.
- [2] L. Mohammed, H.G. Gomaa, D. Raga, J. Zhu, Magnetic nanoparticles for environmental and biomedical applications: a review, *Particuology* 30 (2017) 1–14, <https://doi.org/10.1016/j.partic.2016.06.001>.
- [3] P. Katikaneani, A.K. Vaddeppally, N.R. Tippana, R. Banavath, S. Kommu, Phase transformation of iron oxide nanoparticles from hematite to magnetite in presence of polyethylene glycol: application as corrosion resistant nanoparticle paints, *J. Nanosc.* (2016), <https://doi.org/10.1155/2016/1328463>.
- [4] F. Reyes-Ortega, A.V. Delgado, E.K. Schneider, B.L.C. Fernandez, G.R. Iglesias, Magnetic nanoparticles coated with a thermosensitive polymer with hyperthermia properties, *Polymers* 10 (2018) 1–15, <https://doi.org/10.3390/polym10010010>.
- [5] K. Pusnik, T. Gorsak, M. Drogenik, D. Makovec, Synthesis of aqueous suspensions of magnetic nanoparticles with the co-precipitation of iron ions in the presence of aspartic acid, *J. Magn. Mater.* 413 (2016) 65–75, <https://doi.org/10.1016/j.jmmm.2016.04.032>.
- [6] W. Wu, X. Xiao, S. Zhang, J. Zhou, L. Fan, F. Ren, C. Jiang, Large-scale and controlled synthesis of iron oxide magnetic short nanotubes: shape evolution, growth mechanism, and magnetic properties, *J. Phys. Chem. C* 114 (2010) 16092–16103, <https://doi.org/10.1021/jp1010154>.
- [7] J. Kudr, Y. Haddad, L. Richtera, Z. Heger, M. Cernak, V. Adam, O. Zitka, Magnetic nanoparticles: from design and synthesis to real world applications, *Nanomaterials* 7 (2017) 1–29, <https://doi.org/10.3390/nano7090243>.
- [8] E. Alp, N. Aydogan, A comparative study: synthesis of superparamagnetic iron oxide nanoparticles in air and N<sub>2</sub> atmosphere, *Colloids Surf. A: Physicochem. Eng. Asp.* 510 (2016) 205–212, <https://doi.org/10.1016/j.colsurfa.2016.06.033>.
- [9] K. Song, W. Kim, C.Y. Suh, D. Shin, K.S. Ko, K. Ha, Magnetic iron oxide nanoparticles prepared by electrical wire explosion for arsenic removal, *Powder Technol.* 246 (2013) 572–574, <https://doi.org/10.1016/j.powtec.2013.06.023>.
- [10] I.V. Beketov, A.P. Safronov, A.I. Medvedev, J. Alonso, G.V. Kurlyandskaya, S.M. Bhagat, Iron oxide nanoparticles fabricated by electric explosion of wire: focus on magnetic nanofluids, *AIP Adv.* 2 (2012) 1–25, <https://doi.org/10.1063/1.4730405>.
- [11] A. Sivkov, E. Naiden, A. Ivashutenko, I. Shanenkov, Plasma dynamic synthesis and obtaining ultrafine powders of iron oxides with high content of  $\alpha$ -Fe<sub>2</sub>O<sub>3</sub>, *J. Magn. Mater.* 405 (2016) 158–168, <https://doi.org/10.1016/j.jmmm.2015.12.072>.
- [12] A. Fojtik, A. Henglein, Laser ablation of films and suspended particles in solvent-formation of cluster and colloid solutions, *Ber. Bunsenges. Phys. Chem.* 97 (1993) 252–254.
- [13] J. Nedderson, G. Chumanov, T.M. Cotton, Laser ablation of metals: a new method for preparing SERS active colloids, *Appl. Spectrosc.* 47 (1993) 1959–1964, <https://doi.org/10.1366/0003702934066460>.
- [14] T.E. Itina, On nanoparticle formation by laser ablation in liquids, *J. Phys. Chem. C* 115 (2011) 5044–5048, <https://doi.org/10.1021/jp1090944>.
- [15] D. Amans, M. Diouf, J. Lam, G. Ledoux, C. Dujardin, Origin of the nano-carbon allotropes in pulsed laser ablation in liquids synthesis, *J. Colloid Interf. Sci.* 489 (2017) 114–125, <https://doi.org/10.1016/j.jcis.2016.08.017>.
- [16] G. Marzun, H. Bonnemann, C. Lehmann, B. Spliethoff, C. Weidenthaler, S. Barcikowski, Role of dissolved and molecular oxygen on Cu and PtCu alloy particle structure during laser ablation synthesis in liquids, *ChemPhysChem* 18 (2017) 1175–1184, <https://doi.org/10.1002/cphc.201601315>.
- [17] W.T. Nichols, T. Sasaki, N. Koshizaki, Laser ablation of a platinum target in water. II. Ablation rate and nanoparticle size distributions, *J. Appl. Phys.* 100 (2006) 1–6, <https://doi.org/10.1063/1.2390641>.
- [18] R. Streubel, S. Barcikowski, B. Gokce, Continuous multigram nanoparticle synthesis by high-power, high-repetition-rate ultrafast laser ablation in liquids, *Opt. Lett.* 41 (2016) 1486–1489, <https://doi.org/10.1364/OL.41.001486>.
- [19] S.I. Ashitkov, S.A. Romashevskii, P.S. Komarov, A.A. Burmistrov, V.V. Zhakhovskii, N.A. Inogamov, M.B. Agranat, Formation of nanostructures under femtosecond laser ablation of metals, *Quant. Electron.* 45 (6) (2015) 547–550, <https://doi.org/10.1070/QE2015v045n06ABEH015771>.
- [20] I.N. Lapin, V.A. Svetlichnyi, Features of the synthesis of nanocolloid oxides by laser ablation of bulk metal targets in solutions, *Proc. SPIE* 9810 (2015) 1–7, <https://doi.org/10.1117/12.2224699>.
- [21] J. Zhang, M. Chaker, D. Ma, Pulsed laser ablation based synthesis of colloidal metal nanoparticles for catalytic applications, *J. Colloid Interf. Sci.* 489 (2017) 138–149, <https://doi.org/10.1016/j.jcis.2016.07.050>.
- [22] E.M. Slavinskaya, T.Y. Kardash, R.V. Gulyaev, O.A. Stonkus, I.N. Lapin, V.A. Svetlichnyi, A.I. Boronin, Metal-support interaction in Pd/CeO<sub>2</sub> model catalysts for CO oxidation: from pulsed laser-ablated nanoparticles to highly-active state of the catalyst, *Catal. Sci. Technol.* 6 (2016) 6650–6666, <https://doi.org/10.1039/C6CY00319B>.
- [23] D. Zhang, J. Liu, P. Li, Z. Tian, C. Liang, Recent advances in surfactant-free, surface-charged, and defect-rich catalysts developed by laser ablation and processing in liquids, *ChemNanoMat* 3 (2017) 512–533, <https://doi.org/10.1002/cnma.201700079>.
- [24] N. Mintcheva, A.A. Aljulaifi, W. Wunderlich, S.A. Kulninch, S. Iwamori, Laser-ablated ZnO nanoparticles and their photocatalytic activity toward organic pollutants, *Materials* 11 (2018) 1–11, <https://doi.org/10.3390/ma11071127>.
- [25] V.A. Svetlichnyi, A.V. Shabalina, I.N. Lapin, D.A. Goncharova, Metal oxide nanoparticle preparation by pulsed laser ablation of metallic targets in liquid, in: D. Yang (Ed.), *Applications of Laser Ablation–Thin Film Deposition, Nanomaterial Synthesis and Surface Modification*, InTech, Croatia, 2016, pp. 245–263 <http://doi.org/10.5772/65430>.
- [26] A. Kanitz, J.S. Hoppius, M. del Mar Sanz, M. Maicas, A. Ostendorf, E.L. Gurevich, Synthesis of magnetic nanoparticles by ultrashort pulsed laser ablation of iron in different liquids, *ChemPhysChem* 18 (2017) 1155–1164, <https://doi.org/10.1002/cphc.201601252>.
- [27] I.A. Sukhov, A.V. Simakin, G.A. Shafeev, G. Viau, C. Garcia, Formation of nanoparticles during laser ablation of an iron target in a liquid, *Quant. Electron.* 42 (2012) 453–456, <https://doi.org/10.1070/QE2012v042n05ABEH014753>.
- [28] A.I. Omelchenko, E.N. Sobol, A.V. Simakin, A.A. Serkov, I.A. Sukhov, G.A. Shafeev, Biofunctional magnetic 'core-shell' nanoparticles generated by laser ablation of iron in liquid, *Laser Phys.* 25 (2015), <https://doi.org/10.1088/1054-660X/25/2/025607>.
- [29] T. Iwamoto, T. Ishigaki, Fabrication of iron oxide nanoparticles using laser ablation in liquids, *J. Phys. Conf. Ser.* 441 (2013), <https://doi.org/10.1088/1742-6596/441/1/012034>.
- [30] D. Zhang, W. Choi, Y. Oshima, U. Wiedwald, S.H. Cho, H.P. Lin, Y.K. Li, Y. Ito, K. Sugioka, Magnetic Fe@FeO<sub>x</sub>, Fe@C and  $\alpha$ -Fe<sub>2</sub>O<sub>3</sub> single-crystal nanoblends synthesized by femtosecond laser ablation of Fe in acetone, *Nanomaterials* 8 (2018), <https://doi.org/10.3390/nano8080631>.
- [31] M. Ullmann, S.K. Friedlander, A. Schmidt-Ott, Nanoparticle formation by laser ablation, *J. Nanoparticle Res.* 4 (2002) 499–509, <https://doi.org/10.1023/A:10228409>.
- [32] Z. Wang, Y. Liu, X. Zeng, One-step synthesis of  $\gamma$ -Fe<sub>2</sub>O<sub>3</sub> nanoparticles by laser ablation, *Powder Technol.* 161 (2006) 65–68, <https://doi.org/10.1016/j.powtec.2005.08.037>.
- [33] V.A. Svetlichnyi, A.V. Shabalina, I.N. Lapin, D.A. Goncharova, D.A. Velikanov, A.E. Sokolov, Study of magnetic nanoparticles obtained via pulsed laser ablation of iron in air, *Appl. Surf. Sci.* (2018), <https://doi.org/10.1016/j.apsusc.2018.08.116>.
- [34] V.A. Svetlichnyi, A.V. Shabalina, I.N. Lapin, Structure and properties of nanocrystalline iron oxide powder prepared by the method of pulsed laser ablation, *Russ. Phys. J.* 59 (2017) 2012–2016, <https://doi.org/10.1007/s11182-017-1008-8>.
- [35] V.A. Svetlichnyi, A.V. Shabalina, I.N. Lapin, D.A. Goncharova, D.A. Velikanov, A.E. Sokolov, Characterization and magnetic properties study for magnetite nanoparticles obtained by pulsed laser ablation in water, *Appl. Phys. A* 123 (2017), <https://doi.org/10.1007/s00339-017-1390-7>.
- [36] K.K. Kim, M. Roy, H. Kwon, J.K. Song, S.M. Park, Laser ablation dynamics in liquid phase: the effects of magnetic field and electrolyte, *J. Appl. Phys.* 117 (2015), <https://doi.org/10.1063/1.4913253>.
- [37] O.R. Musae, E.A. Sutter, J.M. Wrobel, M.B. Kruger, The effect of magnetic fields on the products of laser ablation, *Appl. Phys. A* 122 (2016), <https://doi.org/10.1007/s00339-016-9636-3>.
- [38] Y. Liang, P. Liu, J. Xiao, H. Li, C. Wang, G. Yang, A microfibre assembly of an iron-carbon composite with giant magnetization, *Sci. Rep.* 3 (2013) 1–9, <https://doi.org/10.1038/srep03051>.
- [39] NIST X-ray Photoelectron Spectroscopy Database, version 4.1, National Institute of Standards and Technology, Gaithersburg, MD. < <http://srdata.nist.gov/xps/> > , 2012.
- [40] E.A. Lashina, E.M. Slavinskaya, N.A. Chumakova, O.A. Stonkus, R.V. Gulyaev, A.I. Stadnichenko, G.A. Chumakov, A.I. Boronin, G.V. Demidenko, Self-sustained oscillations in CO oxidation reaction on PdO/Al<sub>2</sub>O<sub>3</sub> catalyst, *Chem. Eng. Sci.* 83 (2012) 149–158, <https://doi.org/10.1016/j.ces.2012.03.020>.
- [41] O.Y. Podyacheva, A.I. Stadnichenko, S.A. Yashnik, O.A. Stonkus, E.M. Slavinskaya, A.I. Boronin, A.V. Puzynin, Z.R. Ismagilov, Catalytic and capacity properties of nanocomposites based on cobalt oxide and nitrogen-doped carbon nanofibers, *Chin. J. Catal.* 35 (2014) 960–969, [https://doi.org/10.1016/S1872-2067\(14\)60099-1](https://doi.org/10.1016/S1872-2067(14)60099-1).
- [42] E.M. Slavinskaya, A.I. Stadnichenko, V.V. Muravyov, T.Y. Kardash, E.A. Derevyannikova, V.I. Zaikovskii, O.A. Stonkus, I.N. Lapin, V.A. Svetlichnyi, A.I. Boronin, Transformation of a Pt–CeO<sub>2</sub> mechanistic mixture of pulsed-laser-ablated nanoparticles to a highly active catalyst for carbon monoxide oxidation, *ChemCatChem* 10 (2018) 2232–2247, <https://doi.org/10.1002/cctc.201702050>.
- [43] M.P. Seah, W.A. Dench, Quantitative electron spectroscopy of surfaces: a standard data base for electron inelastic mean free paths in solids, *Surf. Interf. Anal.* 1 (1979) 2–11, <https://doi.org/10.1002/sia.74001103>.
- [44] O.N. Shebanova, P. Lazor, Raman study of magnetite (Fe<sub>3</sub>O<sub>4</sub>): laser-induced thermal effects and oxidation, *J. Raman Spectrosc.* 34 (2003) 845–852, <https://doi.org/10.1002/jrs.1056>.
- [45] T. Yamashita, P. Hayes, Analysis of XPS spectra of Fe<sup>2+</sup> and Fe<sup>3+</sup> ions in oxide

- materials, *Appl. Surf. Sci.* 254 (2008) 2441–2449, <https://doi.org/10.1016/j.apsusc.2007.09.063>.
- [46] N.S. McIntyre, D.G. Zetaruk, X-ray photoelectron spectroscopic studies of iron oxides, *Anal. Chem.* 49 (1977) 1521–1529.
- [47] M. Kosmulski, Surface Charging and Points of Zero Charge, *Surfactant Science Series*, CRC Press, Boca Raton, 1956.
- [48] M. Krajewski, K. Brzozka, M. Tokarczyk, G. Kowalski, S. Lewinska, A. Slawska-Waniewska, W.S. Lin, H.M. Lin, Impact of thermal oxidation on chemical composition and magnetic properties of iron nanoparticles, *J. Magn. Magn. Mater.* 458 (2018) 346–354, <https://doi.org/10.1016/j.jmmm.2018.03.047>.